

# Digital Coincidence Processing for the RatCAP Conscious Rat Brain PET Scanner

S.-J. Park, S. Southehal, M. Purschke, S. S. Junnarkar, J.-F. Pratte, S. P. Stoll, C. L. Woody, D. J. Schlyer, and P. Vaska

**Abstract**—The RatCAP has been designed and constructed to image the awake rat brain. In order to maximize system performance, offline digital coincidence data processing algorithms including offset delay correction and prompt and delayed coincidence detection have been developed and validated. With offset delay correction using a singular value decomposition (SVD) technique, overall time resolution was improved from 32.6 to 17.6 ns FWHM. The experimental results confirm that the ratio of prompts to randoms was improved because a narrower timing window could be used.  $^{18}\text{F}$ -fluoride rat bone scan data were reconstructed using our fully 3-D ML-EM algorithm with a highly accurate detector response model created from Monte Carlo simulation.

**Index Terms**—Awake rat, offset delay correction, RatCAP, singular value decomposition (SVD).

## I. INTRODUCTION

NEUROSCIENCE research demands an advanced preclinical imaging instrument to study animal models of neurotransmitter systems, brain development, and functional mechanisms. However, anesthesia which is commonly used in preclinical imaging studies to prevent motion artifacts produces a profound effect on brain function [1]–[6]. It remains challenging to image the awake animal brain using the current generation of animal PET imagers. With novel technology which allows miniaturization of PET components, the RatCAP has been designed and constructed to image the awake rat brain as shown in Fig. 1 [7]–[10].

The RatCAP consists of a 4 cm I.D. ring of 12 LSO detector blocks. Fig. 2 shows the internal RatCAP components. Each block comprises a  $4 \times 8$  array of  $2 \times 2 \times 5 \text{ mm}^3$  LSO crystals coupled to a  $4 \times 8$  avalanche photodiode array (Hamamatsu S8550 APD) for individual readout from each crystal using a custom-designed front-end Application Specific Integrated Circuit (ASIC) [11]. The output signals from the ASIC are processed in a Field Programmable Gate Array (FPGA) based Time to Digital Converter (TDC) and Signal Processing Module (TSPM) [12]. The digitized single event information (64 bits) including block ID (4 bits), crystal or channel ID (5 bits),

Manuscript received March 29, 2007; revised October 6, 2007. This work was supported by the U.S. Department of Energy (OBER) under Prime Contract DE-AC02-98CH10886.

S.-J. Park, M. Purschke, S. S. Junnarkar, J.-F. Pratte, S. P. Stoll, C. L. Woody, D. J. Schlyer, and P. Vaska are with Brookhaven National Laboratory, Upton, NY 11973 USA (e-mail: sangjune.park@gmail.com).

S. Southehal is with the Biomedical Engineering Department, Stony Brook University, Stony Brook, NY 11794 USA.

Color versions of one or more of the figures in this paper are available online at <http://ieeexplore.ieee.org>.

Digital Object Identifier 10.1109/TNS.2007.912876

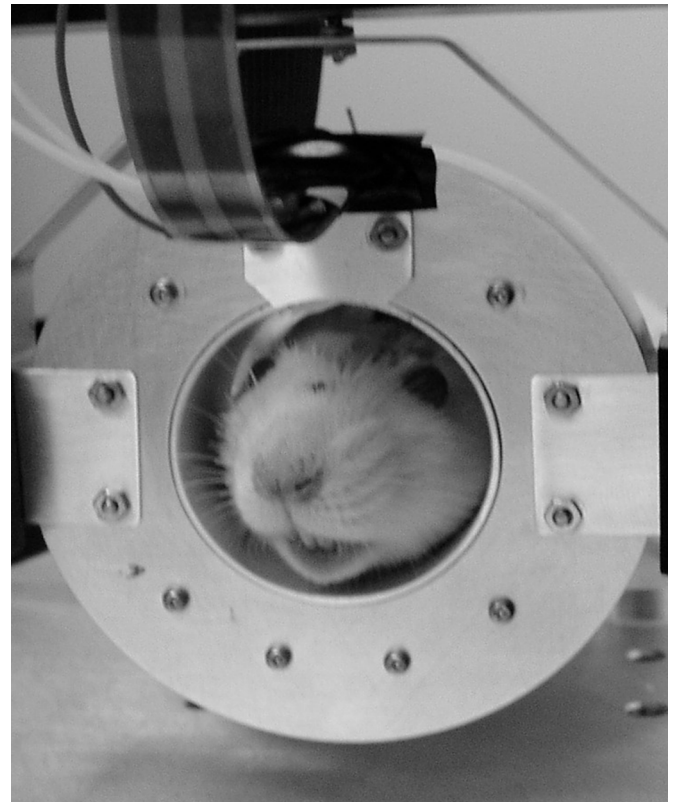


Fig. 1. RatCAP scanner on the head of a rat.

and timestamp (43 bits) is transmitted to a VME-based data acquisition (DAQ) system or an improved optical DAQ system that has recently been developed.

Initial performance tests have shown that the RatCAP has a spatial resolution of 1.8 mm FWHM at the center of the field of view (FOV), energy resolution of 23% FWHM at 511 keV, and sensitivity of 0.7% at an average lower energy threshold of 150 keV [10].

In this paper, we will describe offline digital coincidence data processing algorithms including offset delay correction, prompt and delay coincidence detection, and how the delayed coincidences are incorporated into a novel iterative image reconstruction approach.

## II. DIGITAL COINCIDENCE DATA PROCESSING

### A. Offset Delay Correction

The signal arrival time at the TDC varies significantly between RatCAP detector channels due mainly to time walk

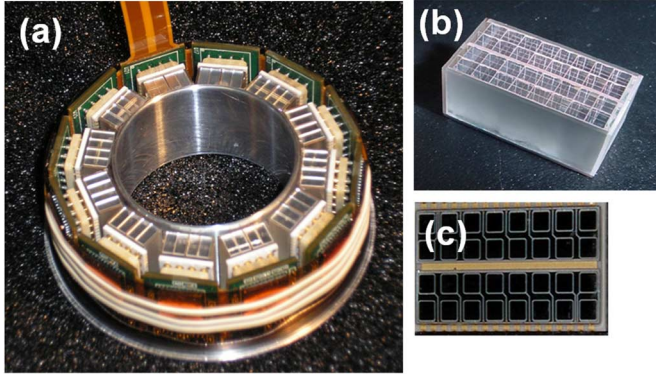


Fig. 2. (a) RatCAP consists of 12 LSO detector blocks and APDs. (b)  $2 \times 2 \times 5$  mm<sup>3</sup> LSO crystals in a  $4 \times 8$  array. (c) Hamamatsu S8550 APD.

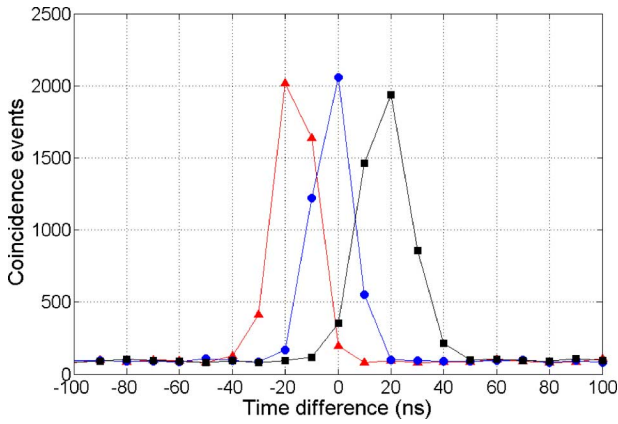


Fig. 3. Timing spectra for three individual coincidence pairs before time offset delay correction. Approximately 8,300 coincidence events per timing spectrum (total  $\sim 600$  million coincidence events/72,192 timing spectra) were measured.

caused by baseline variations in the ASIC triggering circuits coupled with gain variations among channels. Therefore, each individual channel has an inherent offset delay. For example, Fig. 3 shows timing spectra for three individual coincidence pairs from the RatCAP before correcting the offset delay. Due to the offset delay in each channel, a wide coincidence timing window is necessary to maintain adequate efficiency for true coincidence events, but at the cost of increased random event acceptance.

In order to achieve the best possible timing performance, the offset delay must be calculated and subtracted from the timestamp of each single event to compensate for differences in signal arrival time. This would minimize the contribution of random coincidence events through the use of a narrower timing window.

Multiple methods have been developed for time calibration. One approach involves successively aligning the centroid locations of the time difference histograms formed by each line of response (LOR) using an orbiting source used for transmission scans [13], [14]. In some cases simplifying assumptions are made and thus an iterative procedure is required to refine the time offset value. This method was implemented for the LabPET (Université de Sherbrooke, Québec, Canada) consisting of LYSO/LGSO phoswich array coupled to APDs [15]. However, depending on implementation details such as which particular detector pairs are used for the calculation and the

convergence properties of iterative schemes, the errors may not be well controlled.

An alternative approach is to use a timing alignment probe (Scanwell Systems, Montreal, Canada) [16], [17]. The probe consists of a  $^{68}\text{Ge}$  or  $^{22}\text{Na}$  source imbedded in a plastic scintillator coupled to a fast PMT. The probe can detect the positrons emitted during the decay of the isotope before they combine with an electron and undergo annihilation. The probe was used to calibrate the MADPET-II animal PET scanner (Technische Universität München, Munich, Germany) based on the one-to-one coupling of LSO crystals to APDs [18]. The main advantage of the probe is that it provides a common reference signal which allows calculation of the offsets in a very straightforward manner. However, the probe data must be somehow integrated into the PET hardware (or otherwise accurately synchronized) and even after this is done, there is a potential to introduce errors due to the different signal paths between real PET data and the signal chain used for the calibration step with the probe.

We introduce a linear least squares approach to robustly estimate the offset delays in one step using data from all detector pairs, which does not require approximations or extra hardware or even a separate calibration scan. It is solved using Singular Value Decomposition (SVD), weighting the data from all coincidence pairs equally. The SVD algorithm is relatively simple and very robust.

In order to derive the individual channel time offsets ( $t_i$ ) from the (pair-wise) coincidence time spectra, we use the simple relation  $t_i - t_j = \Delta t_{i,j}$ , where  $\Delta t_{i,j}$  is the offset of the prompt coincidence peak for crystal pair  $(i,j)$ . For all 384 crystals in the RatCAP, this can be written in matrix form as:

$$\begin{bmatrix} \text{ch1} & \text{ch2} & \cdots & \text{ch384} & t_i & \Delta t_{i,j} \\ \begin{bmatrix} 1 & -1 & 0 & \cdots & 0 & 0 & 0 \\ 1 & 0 & -1 & \cdots & 0 & 0 & 0 \\ & & & \vdots & & & \\ 0 & 0 & 0 & \cdots & 1 & 0 & -1 \\ 0 & 0 & 0 & \cdots & 0 & 1 & -1 \end{bmatrix} & \bullet & \begin{bmatrix} t_1 \\ \vdots \\ \vdots \\ t_{384} \end{bmatrix} & = & \begin{bmatrix} \Delta t_{1,2} \\ \Delta t_{1,3} \\ \vdots \\ \vdots \\ \Delta t_{383,384} \end{bmatrix} \end{bmatrix} \quad (1)$$

This set of linear algebraic equations for the timing differences can be expressed in simplified matrix form as

$$A \cdot x = b. \quad (2)$$

The raised dot refers to matrix multiplication.  $A$  is the  $m \times n$  matrix of coefficients ( $m = 72,192$  the total number of coincidence pairs among  $n = 384$  channels).  $b$  is a column vector containing timing differences ( $\Delta t_{i,j}$ ) measured from coincidence pair time difference spectra.  $x$  is a column vector containing the channel delays ( $t_i$ ) to be calculated. The coefficient matrix,  $A$ , can be decomposed uniquely using the SVD as

$$A = U \cdot W \cdot V^T \quad (3)$$

where  $U$  ( $V$ ) is an  $m \times m$  ( $n \times n$ ) orthogonal matrix of which columns are eigenvectors of  $AA^T$  ( $A^T A$ ).  $W$  is an  $m \times n$  diag-

onal matrix,  $[\text{diag}(w_j)]$ , containing the singular values ( $w_j$ ) of  $A$ . Then the offset delay can be calculated with

$$x = A^{-1} \cdot b = V \cdot \left[ \text{diag} \left( \frac{1}{w_j} \right) \right] \cdot U^T \cdot b. \quad (4)$$

To estimate the offset delay of each channel using the SVD, coincidence data were measured using a uniform water phantom (3.8 cm dia.  $\times$  2.3 cm length) which precisely filled the entire FOV with activity. The phantom was filled with  $\sim 200 \mu\text{Ci}$  of  $^{18}\text{F}$ -FDG solution. Prompt coincidence pairs were measured at an average lower energy threshold of 150 keV. Time differences from the prompt coincidence pairs were histogrammed to generate 72,192 (the total number of 3-D sinogram bins) timing spectra. The mean time differences were extracted using a Gaussian fit to the timing spectra. If all of the timing spectra are used in the calculation, the size of  $A$  would be 55 megabytes (MB) using 2-byte integer variables (or 28 MB with 1-byte integers). This can be significantly reduced to 1.7 MB using a sparse matrix since there are only two nonzero elements in the each row of  $A$ , with values of 1 and  $-1$ . However, the size of  $U$  would be 42 gigabytes (72,192  $\times$  72,192 matrix  $\times$  8-byte double precision variables) since it has almost no zero elements. By using a portion of coincidence pairs (7,680) which correspond to the LORs from a small FOV (specifically the 10 central columns of the sinogram, or  $\sim 1$  cm dia.), the size of  $U$  was reduced to 470 MB with 8-byte double precision variables. Thus, while all 384 crystals were included in the fit, only the central LORs were used in order to make the problem tractable with this method.

### B. Prompt Coincidence Detection

After subtracting the appropriate offset delay from the time-stamp for each event, the singles were sorted into increasing time order and time differences between successive single events were histogrammed to create an overall spectrum. Timing window width ( $2\tau$ ) was selected to recover the most prompt coincidences ( $2\tau \approx \text{FWTM}$  of the spectrum) while minimizing the acceptance of randoms. When exactly one single event occurred within  $\pm\tau$  from another single, both singles were accepted as a prompt coincidence and assigned into a 3-D sinogram or Michelogram using a lookup table which converts the coincidence pairs (block and crystal IDs) to the sinogram bin address. Since in the digital case, the bin for timing difference = 0 is included in the window, the total digital timing window is  $2\tau + 1$  bins wide in the timing spectrum. For example,  $\tau = 20$  ns and a bin width = 10 ns will give a 50 ns width timing window. Fig. 4 illustrates the width of digital timing window for prompt coincidence detection.

### C. Random Coincidence Estimation

There are three basic methods [19] for random background subtraction: (1) the profile distribution method, (2) delay coincidence method, and (3) countrate method. Since with the RatCAP, the FOV is almost filled with the object as shown in Fig. 1, it is almost impossible to use the profile distribution method in which the tails of the projection data outside the object are used to fit both random and scatter background. The delayed coincidence method was chosen for the RatCAP data processing. Since all singles data were saved and processed offline

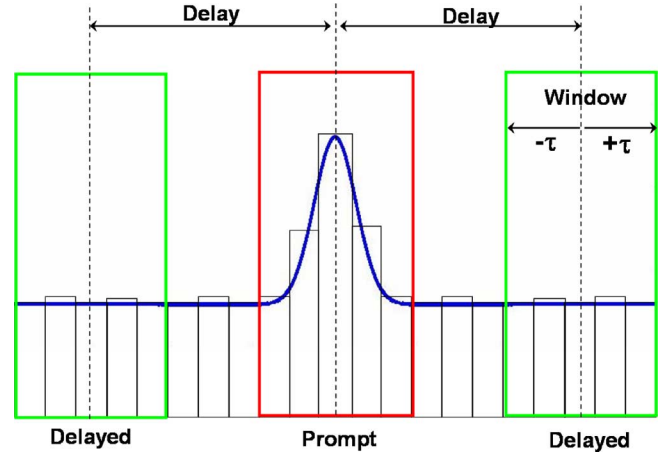


Fig. 4. Prompt and delayed coincidence windows (width = 50 ns using  $\tau = 20$  ns and 10 ns/bin) on a timing spectrum.

in the RatCAP architecture, the double counting of randoms in the prompt and delayed windows does not result in increased deadtime that sometimes occurs with hardware coincidence processors. However, this method suffers from significant statistical noise.

In the conventional delayed-coincidence scheme, the events from one detector of a coincidence detector pair are delayed with an electronic delay circuit. However, in the simplest implementation for time-stamped RatCAP singles data, all singles would be delayed for random detection which gives a factor of 2 too high randoms measurement (see Fig. 4). There are a number of ways to account for this. A simple scaling down of the randoms counts by a factor of 2 is perhaps the simplest. Narrowing the time window for delayed coincidences by a factor of 2 would seem to be another option, but this is not precisely possible with digital time data—as noted above, symmetric time windows must have an odd number of time bins due to the central (zero time difference) bin. We chose the third option of choosing to delay one specific channel of each pair in order to most closely mimic the traditional electronic scheme which produces integer data with no scale factors.

### D. Image Reconstruction

The image reconstruction algorithm is specified in (5). This is the update equation for the 3-D MLEM algorithm with normalization (detector efficiency) and random correction [20]. A system matrix ( $\sim 2$  gigabytes) containing an accurate detector response was calculated using intensive Monte Carlo simulations based on the SimSET package [21].

The image reconstruction algorithm is given in (5) as

$$\lambda_j^{n+1} = \frac{\lambda_j^n}{\sum_i p_{ij} \varepsilon_i} \sum_i p_{ij} \varepsilon_i \frac{Y_i}{\left( \sum_k p_{ik} \lambda_k^n \right) \varepsilon_i + R_i} \quad (5)$$

where  $\lambda$  is the estimate of the image or activity distribution and  $Y_i$  is the prompt coincidence sinogram (projection data in 3-D sinogram).  $P_{ij}$  is the system matrix generated from the Monte Carlo simulations including positron range and the non-collinearity of the annihilation photons. Both attenuation and

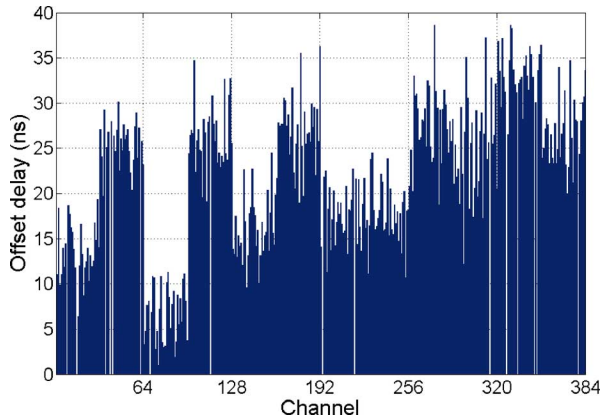


Fig. 5. Calculated offset delays from the 384 channels. The zero offset delay was given for the 16 dead channels (9, 16, 37, 40, 42, 62, 69, 113, 194, 217, 315, 327, 335, 347, 349, and 379).

object scatter were also included in the simulation using an attenuation map (3-D CT images) obtained from a high resolution microCT (SkyScan-1076) of a rat head. Ideally, the system matrix should be generated for each individual animal to accurately take into account attenuation and scatter in the object. However, we used the same system matrix for all the animals of a given strain and weight since we found that this causes no significant variation in region-of-interest (ROI) values except the Poisson photon statistics [20].  $\varepsilon_1$  is a normalization parameter for detector efficiency measured using the uniform phantom and  $R_i$  is the random coincidence sinogram obtained using the delayed coincidence window.  $n$  is the iteration number.

Image data were acquired from rat bone scan. A rat was anesthetized and injected with  $580 \mu\text{Ci}$  of  $^{18}\text{F}$ -fluoride. Images from the RatCAP were reconstructed with the offset delay and random corrections using the 3-D MLEM algorithm.

### III. RESULTS

By using the SVD algorithm, we could directly estimate the offset delay with the single list-mode data itself acquired from the animal scan. It is not even necessary to take an extra scan for time calibration before scanning the animal if there are enough coincidence events to indicate the centroids of the timing spectra. One potential drawback of the method is that it may require a significant amount of computer memory. However, this problem was easily solved by managing matrix size as discussed in Section II-A.

The offset delays of the 384 channels in the RatCAP were calculated using coincidence data obtained from the uniform phantom and the SVD method described above. Fig. 5 shows that the offset delays are distributed over a range of 0–40 ns. It is obvious that twelve groups can be identified on the Fig. 5 since there were gain differences among the twelve different APDs. A scatter plot of the calculated time differences ( $t_i - t_j$ ) versus the measured time differences ( $\Delta t_{i,j}$ ) is shown in Fig. 6. The histogram of the differences ( $(t_i - t_j) - \Delta t_{i,j}$ ) between the measured time differences and the calculated time differences

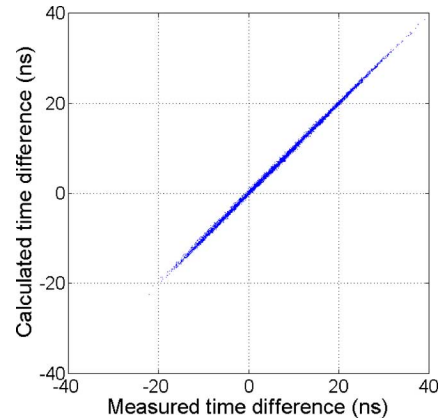


Fig. 6. Scatter plot of the calculated time differences ( $t_i - t_j$ ) versus the measured time differences ( $\Delta t_{i,j}$ ).

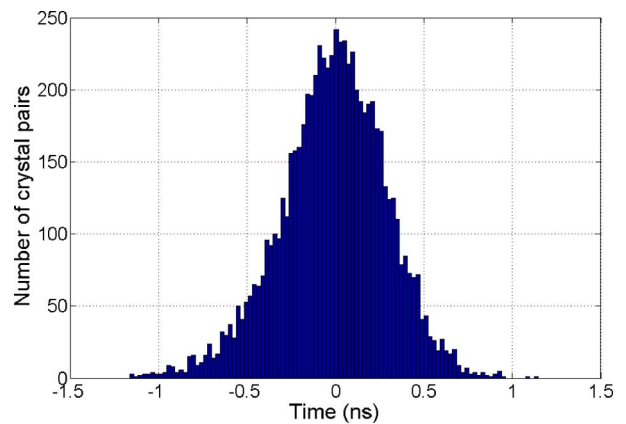


Fig. 7. Histogram of the differences ( $(t_i - t_j) - \Delta t_{i,j}$ ) between the measured time differences ( $\Delta t_{i,j}$ ) and the calculated time differences ( $t_i - t_j$ ). The distribution has a 0.84 ns FWHM and  $\sigma = 0.30$  ns.

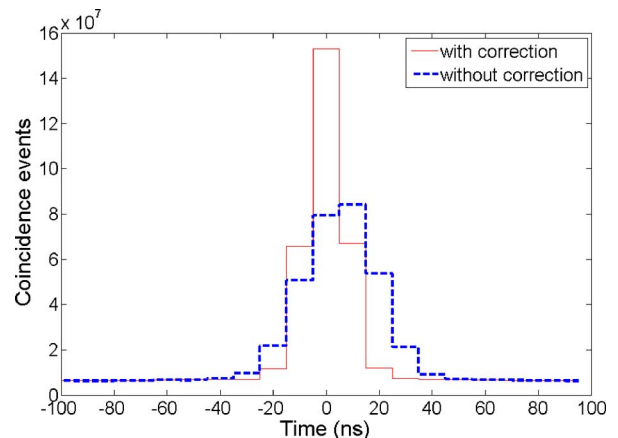


Fig. 8. Timing spectra summing all coincidence timing spectra with and without the offset delay correction.

in Fig. 7 shows the excellent agreement between the two quantities, with a FWHM of 0.84 ns (RMS = 0.30 ns).

Fig. 8 illustrates that before correction, the sum of all timing spectra has a peak shifted to +5.4 ns and rather wide (FWHM = 32.6 ns). After the correction, we measured a timing resolution of 17.6 ns FWHM and a centroid at 0.04 ns

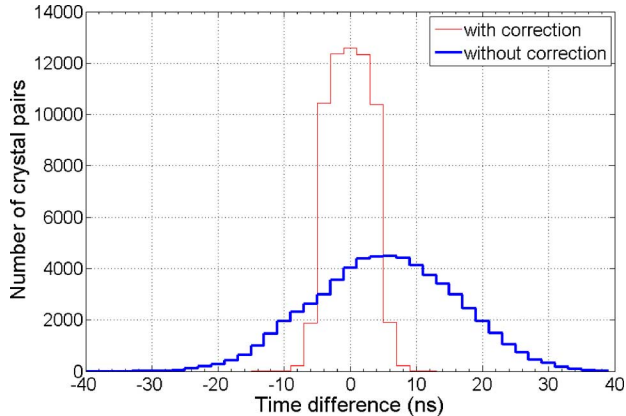


Fig. 9. Distribution of mean time differences. The mean time differences were extracted using a Gaussian fit to each of the 72,192 coincidence timing spectra with and without the offset delay correction.

from the spectrum using a Gaussian fit. Note that we have developed a  $\sim 1.1$  ns bin TDC for time stamping [12] but that a 10 ns bin was used for timestamps in this study since this feature is under development. The mean time differences were extracted using a Gaussian fit to each of the 72,192 coincidence timing spectra with and without the offset delay correction and histogrammed with 2 ns bin width in Fig. 9. The results indicate that the offset delay correction is absolutely necessary to avoid the wide timing distribution and improve the system performance. The offset delays were accurately estimated with the SVD.

Without the offset delay correction, a wide coincidence timing window is necessary in order to maintain adequate efficiency for true coincidence events. From the rat  $^{18}\text{F}$ -fluoride bone scan, the total number of prompt (random) coincidences was measured to be 3,662,485 (376,403) using a wide timing window (50 ns) without the offset delay correction. With the correction using the same timing window, the total number of prompt (random) coincidences was measured to be 3,816,652 (374,848). There is 4.2% gain in the prompts. However, the ratio of the prompts to the randoms is not significantly improved using the correction since the most of true coincidence events were measured using the wide timing window.

With the offset delay correction using a narrower coincidence timing window (30 ns), the total number of prompt (random) coincidences was measured to be 3,142,636 (226,902). The total randoms decrease 40% with reducing the window width to 30 ns. The ratio (0.6 or 3/5) from the number of randoms measured by using the narrow and wide timing windows is in excellent agreement with the ratio (30 ns/50 ns) from their widths. The total prompts also decrease 18% along with the randoms. However, the ratio of prompts to randoms was improved from 10:1 to 14:1.

Fig. 10(a) shows  $^{18}\text{F}$ -Fluoride rat bone scan image from the RatCAP reconstructed with the 3-D MLEM algorithm (20 iterations). Image data was processed with the 30 ns timing window. Randoms and offset delay were corrected. Skull and jaw-bones are clearly visible in the image. The ring artifact on the image

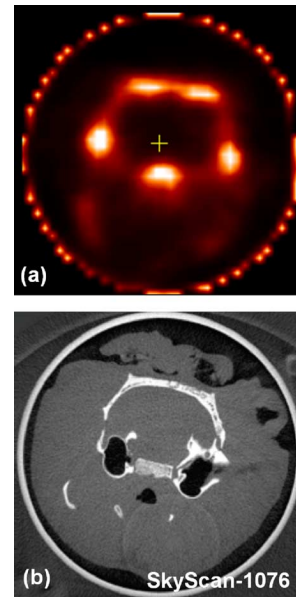


Fig. 10. (a)  $^{18}\text{F}$ -Fluoride rat bone scan image (4 cm  $\times$  4 cm) from the RatCAP reconstructed with the 3-D MLEM algorithm (20 iterations, 30 ns timing window, randoms and offset delay are corrected.). The ring artifact on the image caused by inter-crystal scatters was not removed intentionally in the data processing to show the full FOV. (b) Image from the microCT (SkyScan-1076) used for the geometry of the Monte Carlo simulations to calculate the system matrix including attenuation and scatter in the object. Note that two different rats of similar size ( $\sim 500$  g) were scanned for (a) and (b).

caused by inter-crystal scatters was not removed intentionally in the data processing in order to show the full FOV. For verification, a high resolution microCT image is represented in Fig. 10(b). The image was used for the geometry of the Monte Carlo simulations to calculate the system matrix including attenuation and scatter in the object. The image shows bone structure with high resolution ( $\sim 10$   $\mu\text{m}$  FWHM). Note that two different rats of similar size ( $\sim 500$  g) were scanned for Fig. 10(a) and (b).

#### IV. CONCLUSION

We have presented digital coincidence data processing for the RatCAP including offset delay correction with a singular value decomposition approach, prompt and random coincidence measurement, and 3-D MLEM image reconstruction. The experimental results confirm that the ratio of prompts to randoms was improved because the offset delay correction allows us to use a narrower timing window.

#### ACKNOWLEDGMENT

The authors would like to thank the members of the Brookhaven PET group for their support with radioisotopes and animal issues.

#### REFERENCES

- [1] S. Momosaki, K. Hatano, Y. Kawasumi, T. Kato, R. Hosoi, K. Kobayashi, O. Inoue, and K. Ito, "Rat-PET study without anesthesia: Anesthetics modify the dopamine D1 receptor binding in rat brain," *Synapse*, vol. 54, pp. 207–13, 2004.

- [2] W. Hassoun, M. Le Cavorsin, N. Ginovart, L. Zimmer, V. Gualda, F. Bonnefoi, and V. Leviel, "PET study of the [(11)C]raclopride binding in the striatum of the awake cat: Effects of anaesthetics and role of cerebral blood flow," *Euro. J. Nucl. Med. Molecular Imag.*, vol. 30, pp. 185–186, 2003.
- [3] H. Tsukada, S. Nishiyama, T. Kakiuchi, H. Ohba, K. Sato, and N. Harada, "Ketamine alters the availability of striatal dopamine transporter as measured by [C-11]beta-CFT and [C-11]beta-CIT-FE in the monkey brain," *Synapse*, vol. 42, pp. 273–280, 2001.
- [4] K. S. Hendrich, P. M. Kochanek, J. A. Melick, J. K. Schiding, K. D. Statler, D. S. Williams, D. W. Marion, and C. Ho, "Cerebral perfusion during anesthesia with fentanyl, isoflurane, or pentobarbital in normal rats studied by arterial spin-labeled MRI," *Magn. Reson. Med.*, vol. 46, pp. 202–206, 2001.
- [5] C. W. Berridge and M. F. Morris, "Amphetamine-induced activation of forebrain EEG is prevented by noradrenergic beta-receptor blockade in the halothane-anesthetized rat," *Psychopharmacol. (Berl)*, vol. 148, pp. 307–313, 2000.
- [6] A. E. Ryabinin, Y. M. Wang, R. K. Bachtell, A. E. Kinney, M. C. Grubb, and G. P. Mark, "Cocaine-and alcohol-mediated expression of inducible transcription factors is blocked by pentobarbital anesthesia," *Brain. Res.*, vol. 877, pp. 251–261, 2000.
- [7] P. Vaska, C. L. Woody, D. J. Schlyer, V. Radeka, P. O'Connor, J.-F. Pratte, S. Shokouhi, S. P. Stoll, S. S. Junnarkar, M. Purschke, S.-J. Park, S. Southekal, V. Dzordzhadze, W. Schiffer, J. Neill, M. Murphy, T. Aubele, R. Kristiansen, A. Villanueva, S. Boose, A. Kandasamy, B. Yu, A. Kriplani, S. Krishnamoorthy, R. Lecomte, and R. Fontaine, "Initial performance of the RatCAP, a PET camera for conscious rat brain imaging," in *Proc. IEEE Nucl. Sci. Symp. Conf. Rec.*, 2005, pp. 3040–3044.
- [8] P. Vaska, C. L. Woody, D. J. Schlyer, S. Shokouhi, S. P. Stoll, J.-F. Pratte, P. O'Connor, S. S. Junnarkar, S. Rescia, B. Yu, M. Purschke, A. Kandasamy, A. Villanueva, A. Kriplani, V. Radeka, N. Volkow, R. Lecomte, and R. Fontaine, "RatCAP: Miniaturized head-mounted PET for conscious rodent brain imaging," *IEEE Trans. Nucl. Sci.*, vol. 51, no. 5, pp. 2718–2722, Oct. 2004.
- [9] C. Woody, A. Kriplani, P. O'Connor, J.-F. Pratte, V. Radeka, S. Rescia, D. Schlyer, S. Shokouhi, S. Stoll, P. Vaska, A. Villanueva, N. Volkow, and B. Yu, "RatCAP: A small, head-mounted PET tomograph for imaging the brain of an awake rat," *Nucl. Instr. Meth. A*, vol. 527, pp. 166–170, 2004.
- [10] C. Woody, P. Vaska, D. Schlyer, J.-F. Pratte, S. Junnarkar, S.-J. Park, S. Stoll, M. Purschke, S. Southekal, A. Kriplani, S. Krishnamoorthy, S. Maramaju, D. Lee, W. Schiffer, S. Dewey, J. Neill, A. Kandasamy, P. O'Connor, V. Radeka, R. Fontaine, and R. Lecomte, "Initial studies using the RatCAP conscious animal PET tomograph," *Nucl. Instr. Meth. A*, vol. 571, pp. 14–17, 2007.
- [11] J.-F. Pratte, G. DeGeronimo, S. Junnarkar, P. O'Connor, B. Yu, S. Robert, V. Radeka, C. Woody, S. Stoll, P. Vaska, A. Kandasamy, R. Lecomte, and R. Fontaine, "Front-end electronics for the RatCAP mobile animal PET scanner," *IEEE Trans. Nucl. Sci.*, vol. 51, no. 4, pp. 1318–1323, Aug. 2004.
- [12] S. S. Junnarkar, M. L. Purschke, J.-F. Pratte, P. O'Connor, and R. Fontaine, "An FPGA-based, 12-channel TDC and digital signal processing module for the RatCAP PET scanner," in *Proc. IEEE Nucl. Sci. Symp. Conf. Rec.*, 2005, pp. 919–923.
- [13] M. W. Lenox, T. Gremillion, S. Miller, and J. W. Young, "Coincidence time alignment for planar pixellated positron emission tomography detector arrays," in *Proc. IEEE Nucl. Sci. Symp. Conf. Rec.*, 2001, pp. 1952–1954.
- [14] D. Luo, J. J. Williams, M. K. Limkeman, M. J. Cook, E. L. Oswald, M. P. Feilen, and D. L. McDaniel, "Crystal-based coincidence timing calibration for PET scanner," in *Proc. IEEE Nucl. Sci. Symp. Conf. Rec.*, 2002, pp. 1676–1680.
- [15] M.-A. Tetrault, N. Viscogliosi, J. Riendeau, F. Belanger, J. B. Michaud, H. Semmaoui, P. Berard, F. Lemieux, L. Arpin, J. Cadorette, C. M. Pepin, G. Robert, M. D. Lepage, R. Lecomte, and R. Fontaine, "System integration of the LabPET™ small animal PET scanner," in *Proc. IEEE Nucl. Sci. Symp. Conf. Rec.*, 2006, pp. 1880–1884.
- [16] C. J. Thompson, M. Camborde, and M. E. Casey, "A central positron source to perform the timing alignment of detectors in a PET scanner," *IEEE Trans. Nucl. Sci.*, vol. 52, no. 5, pp. 1300–1304, Oct. 2005.
- [17] W. W. Moses and C. J. Thompson, "Timing calibration in PET using a time alignment probe," *IEEE Trans. Nucl. Sci.*, vol. 53, no. 5, pp. 2660–2665, Oct. 2006.
- [18] D. P. McElroy, C. J. Thompson, V. Spanoudaki, and S. I. Ziegler, "Use of a central positron emitting reference source to improve the timing alignment of a singles list-mode small animal PET scanner," *IEEE Trans. Nucl. Sci.*, vol. 54, no. 1, pp. 50–54, Feb. 2007.
- [19] R. J. Smith and J. S. Karp, "A practical method for random subtraction in volume imaging PET from detector singles count-rate measurements," *IEEE Trans. Nucl. Sci.*, vol. 43, no. 3, pp. 1981–1987, Jun. 1996.
- [20] S. Southekal, M. Purschke, S.-J. Park, S. S. Junnarkar, J.-F. Pratte, S. P. Stoll, V. Boronikolas, D. E. Lee, D. J. Schlyer, C. L. Woody, and P. Vaska, "Quantitative image reconstruction for the RatCAP PET scanner," in *Proc. IEEE Nucl. Sci. Symp. Conf. Rec.*, 2006, pp. 2736–2739.
- [21] T. K. Lewellen, R. L. Harrison, and S. Vannoy, "The SimSET program," in *Monte Carlo Calculations in Nuclear Medicine, Medical Science Series*, M. Liungberg, S.-E. Strand, and M. A. King, Eds. Bristol, U.K.: Inst. Physics, 1998, pp. 77–92.